



A Rapidly Declining Transient Discovered with the Subaru/Hyper Suprime-Cam

Nozomu Tominaga^{1,2}, Tomoki Morokuma^{2,3}, Masaomi Tanaka^{2,4}, Naoki Yasuda², Hisanori Furusawa⁴, Masayuki Tanaka⁴, Ji-an Jiang^{2,3}, Alexey Tolstov⁵, Sergei Blinnikov^{6,7}, Mamoru Doi^{3,8}, Ikuru Iwata^{9,10,11}, Hanindyo Kuncarayakti^{12,13}, Takashi J. Moriya⁴, Tohru Nagao¹⁴, Ken'ichi Nomoto², Junichi Noumaru¹⁰, and Tadamfumi Takata⁴

¹ Department of Physics, Faculty of Science and Engineering, Konan University, 8-9-1 Okamoto, Kobe, Hyogo 658-8501, Japan; tominaga@konan-u.ac.jp

² Kavli Institute for the Physics and Mathematics of the Universe (WPI), The University of Tokyo, 5-1-5 Kashiwanoha, Kashiwa, Chiba 277-8583, Japan

³ Institute of Astronomy, Graduate School of Science, The University of Tokyo, 2-21-1 Osawa, Mitaka, Tokyo 181-0015, Japan

⁴ Astronomical Institute, Tohoku University, Aoba, Sendai, Miyagi 980-8578, Japan

⁵ The Open University of Japan, 2-11, Wakaba, Mihama-ku, Chiba, Chiba 261-8586, Japan

⁶ NRC “Kurchatov institute”—ITEP, Moscow 117218, Russia

⁷ SAI MSU Moscow 119234, Russia

⁸ Research Center for the Early Universe, Graduate School of Science, The University of Tokyo, 7-3-1, Hongo, Bunkyo-ku, Tokyo 113-003, Japan

⁹ The Graduate University for Advanced Studies (SOKENDAI), Tokyo 181-8588, Japan

¹⁰ Subaru Telescope, National Astronomical Observatory of Japan, 650 North A’ohoku Place, Hilo, HI 96720, USA

¹¹ Department of Astronomy and Physics and Institute for Computational Astrophysics, Saint Mary’s University, 923 Robie Street, Halifax, Nova Scotia B3H 3C 3, Canada

¹² Finnish Centre for Astronomy with ESO (FINCA), FI-20014 University of Turku, Finland

¹³ Tuorla Observatory, Department of Physics and Astronomy, FI-20014 University of Turku, Finland

¹⁴ Research Center for Space and Cosmic Evolution, Ehime University, Bunkyo-cho, Matsuyama 790-8577, Japan

Received 2019 April 27; revised 2019 August 17; accepted 2019 September 5; published 2019 October 24

Abstract

We perform a high-cadence transient survey with the Subaru Hyper Suprime-Cam (HSC), which we call the Subaru HSC survey Optimized for Optical Transients (SHOOT). We conduct HSC imaging observations with time intervals of about one hour on two successive nights, and spectroscopic and photometric follow-up observations. A rapidly declining blue transient SHOOT14di at $z = 0.4229$ is found in observations on two successive nights using an image-subtraction technique. The rate of brightness change is $+1.28_{-0.27}^{+0.40}$ mag day⁻¹ ($+1.83_{-0.39}^{+0.57}$ mag day⁻¹) in the observer (rest) frame and the rest-frame color between 3400 and 4400 Å is $M_{3400 \text{ Å}} - M_{4400 \text{ Å}} = -0.4$. The nature of the object is investigated by comparing its peak luminosity, decline rate, and color with those of transients and variables previously observed, and with those of theoretical models. None of the transients or variables share the same properties as SHOOT14di. Comparisons with theoretical models demonstrate that, while the emission from the cooling envelope of a SN IIb shows a slower decline rate than SHOOT14di, and the explosion of a red supergiant star with a dense circumstellar wind shows a redder color than SHOOT14di, the shock breakout at the stellar surface of the explosion of a $25M_{\odot}$ red supergiant star with a small explosion energy of $\leq 0.4 \times 10^{51}$ erg reproduces the multicolor light curve of SHOOT14di. This discovery shows that a high-cadence, multicolor optical transient survey at intervals of about one hour, and continuous and immediate follow-up observations, is important for studies of normal core-collapse supernovae at high redshifts.

Key words: radiative transfer – shock waves – stars: evolution – supernovae: general – supernovae: individual (SHOOT14di) – surveys

1. Introduction

Traditional transient surveys have been performed mainly with a cadence of several days to catch large numbers of SNe Ia. Searching the transient sky in a shorter timescale has gained attention as a new frontier of astronomy in this decade. In particular, timescales as short as 1 day have been intensively investigated by transient surveys with wide-field cameras, e.g., the Palomar Transient Factory (PTF; Law et al. 2009; Rau et al. 2009) and Zwicky Transient Facility (Graham et al. 2019) with a 1.2 m telescope, the Catalina Real-Time Transient Survey with a 0.7 m telescope (CRTS; Drake et al. 2009), the KisoSupernova Survey with a 1 m telescope (KISS; Morokuma et al. 2014), and the High-cadence Transient Survey with a 4 m telescope (HiTS; Förster et al. 2016).

Several phenomena are theoretically proposed to appear in ultraviolet and optical bands at the short timescale of $\lesssim 1$ day, and these will offer new insights, especially on the final stages of the evolution of massive stars. For example, the emission from a

shock breakout at the stellar surface (Klein & Chevalier 1978) and in the dense wind (Chevalier & Irwin 2011) and subsequent emission from the cooling envelopes (Waxman et al. 2007; Nakar & Sari 2010) of core-collapse supernovae of red supergiant stars, have characteristic timescales of 1 hr to several days. Studying such transients will reveal the stellar radius and the structure of the circumstellar medium surrounding the progenitor star, and thus the mass loss just before the core collapse.

Ultraviolet observations with the *Galaxy Evolution Explorer* (GALEX) satellite (Morrissey et al. 2005, 2007) reveal a brightening at the position of Type II plateau supernovae; SNLS-04D2dc ($z = 0.185$, Gezari et al. 2008; Schawinski et al. 2008), SNLS-06D1jd ($z = 0.324$, Gezari et al. 2008), and PS1-13arp ($z = 0.1665$, Gezari et al. 2015). The UV brightening of SNLS-04D2dc is well reproduced by the emission of the shock breakout at the stellar surface of a star with a zero-age main-sequence mass M_{ZAMS} of $20M_{\odot}$, solar metallicity, i.e., $R_{\text{preSN}} = 800R_{\odot}$, and a canonical explosion energy $E = 1.2 \times 10^{51}$ erg (Tominaga et al. 2009). Also, a rapid rise detected by the *Kepler*

Table 1
Subaru Observations and Light Curves of SHOOT14di

UT	MJD	Epoch	Instrument	Filter	Exposure Time (s)	Flux ^a (μ Jy)	Flux Error ^a (μ Jy)	AB Magnitude (mag)	Significance (σ)	Seeing ^b (arcsec)
2014 Jul 2	56840.554	Day 1	HSC	<i>g</i>	600	0.289	0.042	25.25 ^{+0.17} _{-0.15}	7.0	0.566
2014 Jul 2	56840.591	Day 1	HSC	<i>g</i>	600	0.277	0.041	25.30 ^{+0.18} _{-0.15}	6.7	0.485
2014 Jul 2	56840.610	Day 1	HSC	<i>g</i>	600	0.358	0.043	25.02 ^{+0.14} _{-0.12}	8.4	0.523
2014 Jul 3	56841.525	Day 2	HSC	<i>g</i>	600	0.056	0.043	>26.11 ^c	1.3	0.665
2014 Jul 3	56841.559	Day 2	HSC	<i>g</i>	600	0.087	0.044	>26.09 ^c	2.0	0.581
2014 Jul 3	56841.596	Day 2	HSC	<i>g</i>	600	0.118	0.040	26.22 ^{+0.45} _{-0.32}	3.0	0.552
2014 Jul 3	56841.615	Day 2	HSC	<i>g</i>	600	0.095	0.057	>25.82 ^c	1.7	0.600
2014 Aug 5	56874.339	Day 35	FOCAS	<i>g</i>	960	0.117	0.090	>25.32 ^c	1.3	0.872
2015 May 24	57166.513	Day 327	HSC	<i>g</i>	960	... ^d	... ^d	... ^d	... ^d	0.950
2014 Jul 2	56840.585	Day 1	HSC	<i>g</i>	1800	0.296	0.036	25.22 ^{+0.14} _{-0.13}	8.1	0.523
2014 Jul 3	56841.574	Day 2	HSC	<i>g</i>	2400	0.092	0.037	26.50 ^{+0.56} _{-0.37}	2.5	0.593
2014 Jul 2	56840.467	Day 1	HSC	<i>r</i>	600	0.214	0.052	25.57 ^{+0.30} _{-0.23}	4.2	0.799
2014 Jul 3	56841.445	Day 2	HSC	<i>r</i>	600	0.092	0.065	>25.68 ^c	1.4	0.545
2014 Aug 5	56874.326	Day 35	FOCAS	<i>r</i>	960	0.052	0.098	>25.23 ^c	0.5	0.950
2015 Aug 19	57253.501	Day 414	HSC	<i>r</i>	1440	... ^d	... ^d	... ^d	... ^d	1.410

Notes.^a Corrected for the Galactic extinction with the color excess of $E_{B-V, Gal} = 0.036$ mag.^b Full width at half maximum.^c Calculated from the 3σ error.^d Used for the reference image.

Table 2
Imaging Observations and Photometry of the Host Galaxy of SHOOT14di

UT	Epoch	Instrument	Filter	Exposure Time (s)	CModel Flux ^a (μ Jy)	Flux Error ^a (μ Jy)	Seeing ^b (arcsec)
2015 May 24	Day 327	HSC	<i>g</i>	960	0.473	0.028	0.950
2015 Aug 19	Day 414	HSC	<i>r</i>	1440	0.743	0.038	1.410
2016 May 7	Day 676	S-Cam	<i>r'</i>	1500	0.678	0.036	1.102
2016 May 7	Day 676	S-Cam	<i>i'</i>	1500	0.814	0.047	0.778
2016 May 7	Day 676	S-Cam	<i>Y</i>	3600	0.902	0.230	0.809

Notes.^a Uncorrected for the Galactic extinction with the color excess of $E_{B-V, Gal} = 0.036$ mag.^b Full width at half maximum.

satellite is also reported for KSN 2011d ($z = 0.087$, Garnavich et al. 2016), but the detection has been questioned by Rubin & Gal-Yam (2017). Recently, the rising part of the shock breakout is firmly detected for the Type IIb SN 2016gkg by a fortunate amateur astronomer, and exhibits a fast rise rate of 43 ± 6 mag day⁻¹ (Bersten et al. 2018). A fast rise rate of 31 mag day⁻¹ is also found in a broad-lined stripped-envelope supernova SN2018gep, and is interpreted as a shock breakout in a massive shell of dense circumstellar medium (CSM; Ho et al. 2019).

On the other hand, the UV emission of PS1-13arp is ~ 1 mag brighter than that of SNLS-04D2dc, and its rise time and duration are $\gtrsim 50$ times longer than the radiative diffusion time and the light-crossing time of the shock breakout at the stellar surface (Gezari et al. 2015), thus the UV burst is interpreted as a shock breakout in a circumstellar wind with high mass-loss rate of $10^{-3} M_{\odot} \text{ yr}^{-1}$. The shock breakout in a dense wind is also proposed for the Type IIIn SN PTF 09uj (Ofek et al. 2010), and its NUV light curve rises with a timescale of a few days to an absolute magnitude of ~ -19.5 mag. Its peak brightness and rapid rise have been attributed to the shock breakout in a dense circumstellar wind with a high mass-loss rate of $\sim 10^{-1} M_{\odot} \text{ yr}^{-1}$.

Furthermore, immediate optical follow-up spectroscopic observations exhibit flash-ionized signatures (Gal-Yam et al. 2014) and reveal that the Type II plateau SN SN 2013fs is surrounded by a dense CSM (Yaron et al. 2017). The signature of dense CSM might appear in the rapid rise in SNe IIP (Morozova et al. 2016), and the variation of the rising timescale might be explained by variations in the dense CSM (Morozova et al. 2017; Moriya et al. 2018). On the other hand, the existence of dense CSM is inconsistent with the UV emission of SNLS-04D2dc. Förster et al. (2018) performed light-curve fitting of the SNe II LC discovered by the HiTS with theoretical models (Moriya et al. 2018) and found that 24 of 26 SNe II have a rapid rise that can be explained by dense CSM with a mass-loss rate of $> 10^{-4} M_{\odot} \text{ yr}^{-1}$. These observations imply variations in the final phases of stellar evolution. High-cadence observations are needed to reveal the final stages of these massive stars.

Therefore, we performed a high-cadence transient survey with Hyper Suprime-Cam (HSC; Miyazaki et al. 2006, 2012)¹⁵ with a

¹⁵ <http://www.subarutelescope.org/Observing/Instruments/HSC/index.html>

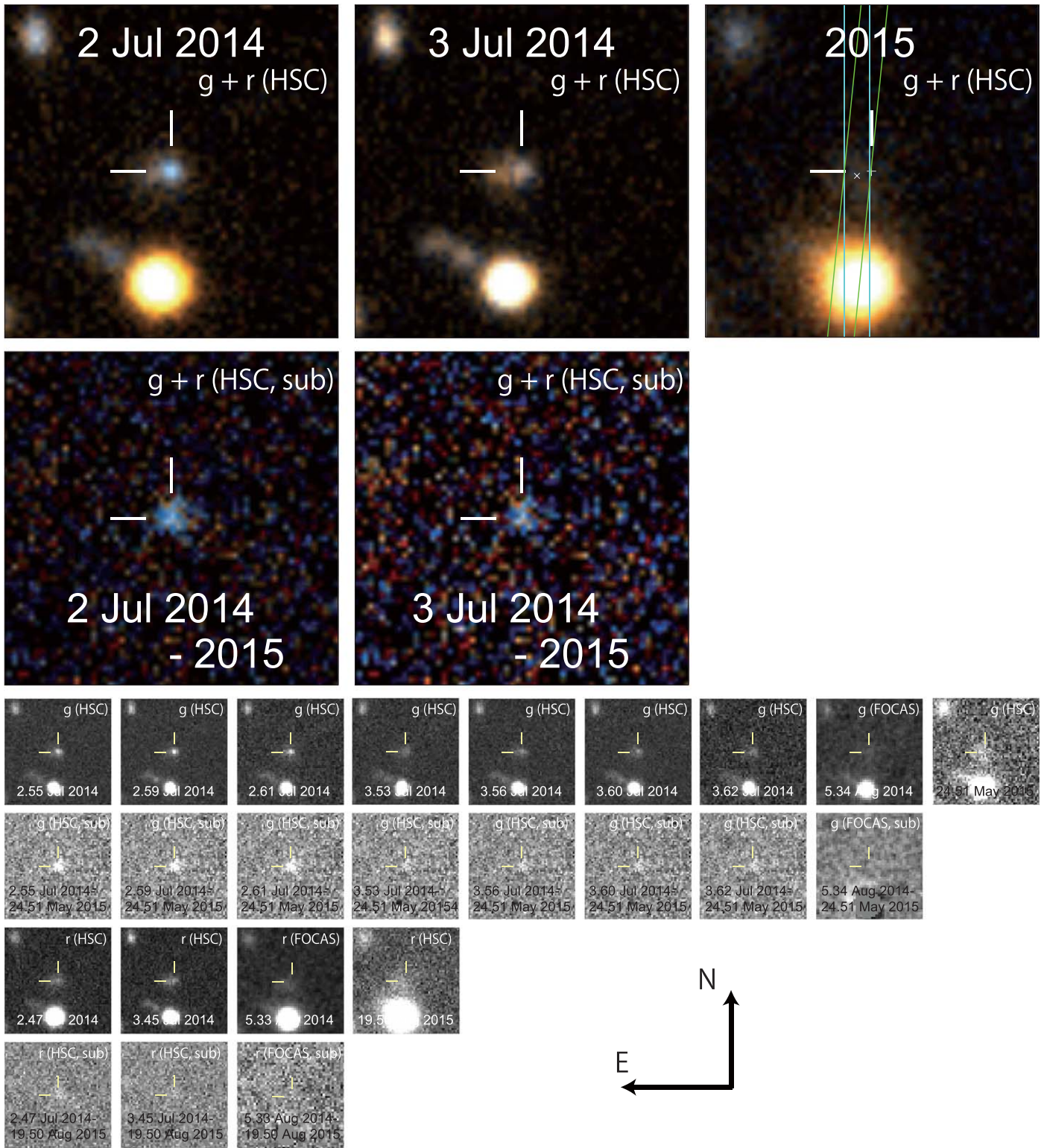


Figure 1. Images at the location of SHOOT14di (ticks). SHOOT14di is located at $0^{\prime\prime}.44$ west and $0^{\prime\prime}.14$ north of the host galaxy with the FWHM size of $1^{\prime\prime}.10$ in the r band. In the multicolor image taken in 2015, the positions of SHOOT14di and the center of the host galaxy are shown with plus and cross, respectively, and the slits for spectroscopic observations with FOCAS and GMOS are shown with green and cyan boxes, respectively. The slit positions are centered at the host galaxy and the position angle are $-13^{\circ}3$ east of north for the FOCAS observation and 0° east of north for the GMOS observation. The lengths of ticks are $1^{\prime\prime}$ and the figure size is 10×10 arcsec².

field of view of 1.77 deg^2 . This is the most powerful instrument, with the highest light-collecting power per unit time, currently available to detect rapid transients. We also conducted follow-up observation as part of a Subaru HSC survey Optimized for Optical Transients (SHOOT). In this paper, we focus on a rapidly

declining transient named SHOOT14di found in the SHOOT 2014 July run; rapidly rising transients from that run are summarized in Tanaka et al. (2016).

This paper consists of following sections. In Section 2, the observations are described. In Section 3, observational properties

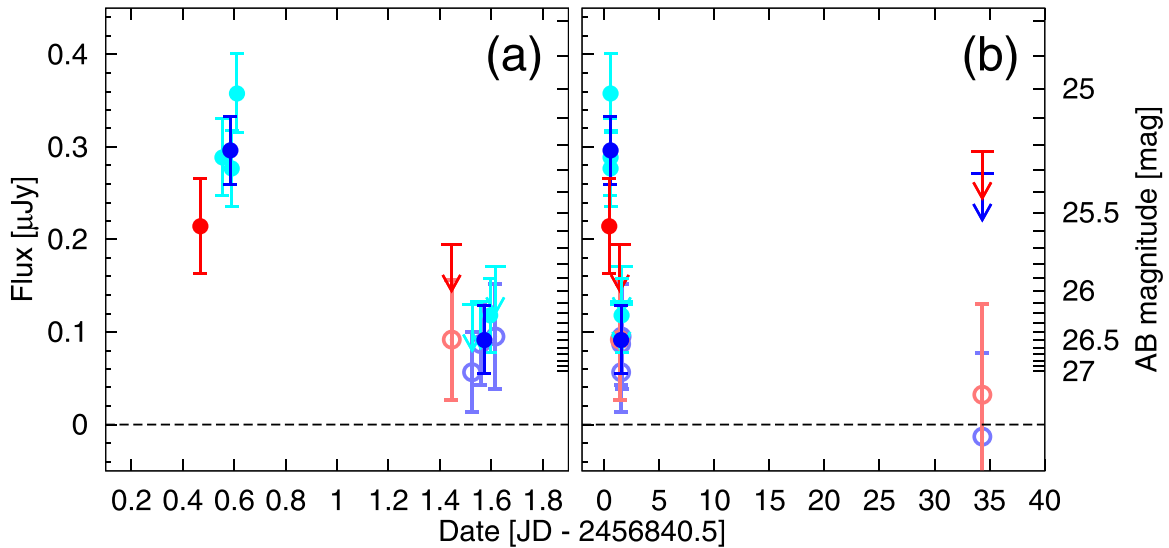


Figure 2. Multicolor light curves of SHOOT14di (cyan, g band [hourly stacked]; blue, g band [daily-stacked]; red, r band) and the redshifted near-UV light curve of SNLS-04D2dc (gray) (a) at the shock breakout phase and (b) from the shock breakout to \sim month after the explosion. The 3σ upper limits and the open symbols are shown at the phase when the significance is low ($\leq 2\sigma$).

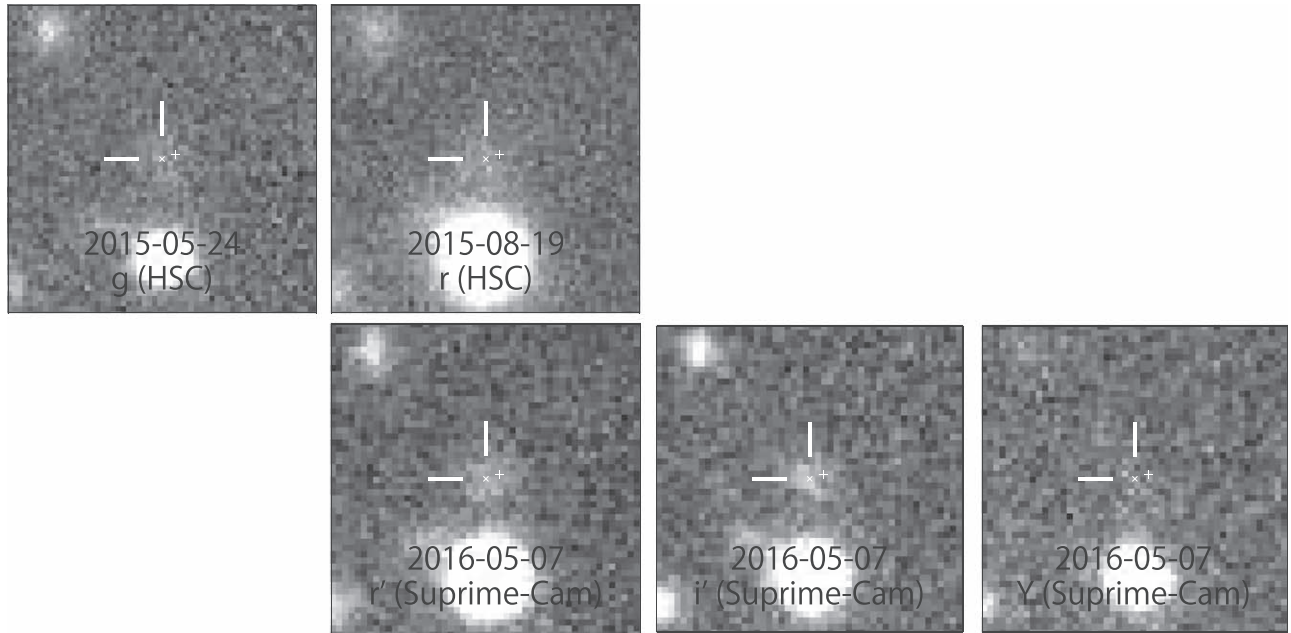


Figure 3. Multicolor images of the host galaxy. The lengths of ticks are $1''$ and the figure size is 10×10 arcsec 2 . The positions of SHOOT14di and the center of the host galaxy are shown with plus and cross, respectively.

of SHOOT14di are summarized. In Sections 4 and 5, these properties of SHOOT14di are compared with those of known transients and variables, and of theoretical models, respectively. In Section 6, we discuss the findings and present our conclusions. In this paper, we adopt the AB magnitude system and the *WMAP5* cosmological parameters: $H_0 = 70.5 \text{ km s}^{-1} \text{ Mpc}^{-1}$, $k = 0$, $\Omega_\lambda = 0.726$, and $\Omega_M = 0.273$ (Komatsu et al. 2009).

2. Observations and Data Reduction

2.1. Imaging Observations of Transients

The g - and r -band imaging observations were carried out on seven fields with HSC on 2014 July 2 and 3 (UT) (Days 1 and 2). In this paper, we focus on a candidate SHOOT14di at

R.A. = $21^{\text{h}}33^{\text{m}}04^{\text{s}}.27$, decl. = $+09^\circ35'55''.0$ (J2000.0) found in one of our survey fields (Figure 1). The field was observed three times in the g band and once in the r band on Day 1, and four times in the g band and once in the r band on Day 2. Each exposure unit on Days 1 and 2 consists of five 2-minute frames with ditherings, and the time intervals between the exposure units are about an hour. We also took g - and r -band images of 16 minutes exposures with Subaru Faint Object Camera And Spectrograph (FOCAS; Kashikawa et al. 2002) on 2014 August 5 (Day 35), a g -band image of 16 minutes exposure with HSC on 2015 May 24 (UT) (Day 327), and an r -band image of 24 minutes exposure with HSC on 2015 August 19 (UT) (Day 414). The details of the imaging observations of transients are summarized in Table 1.

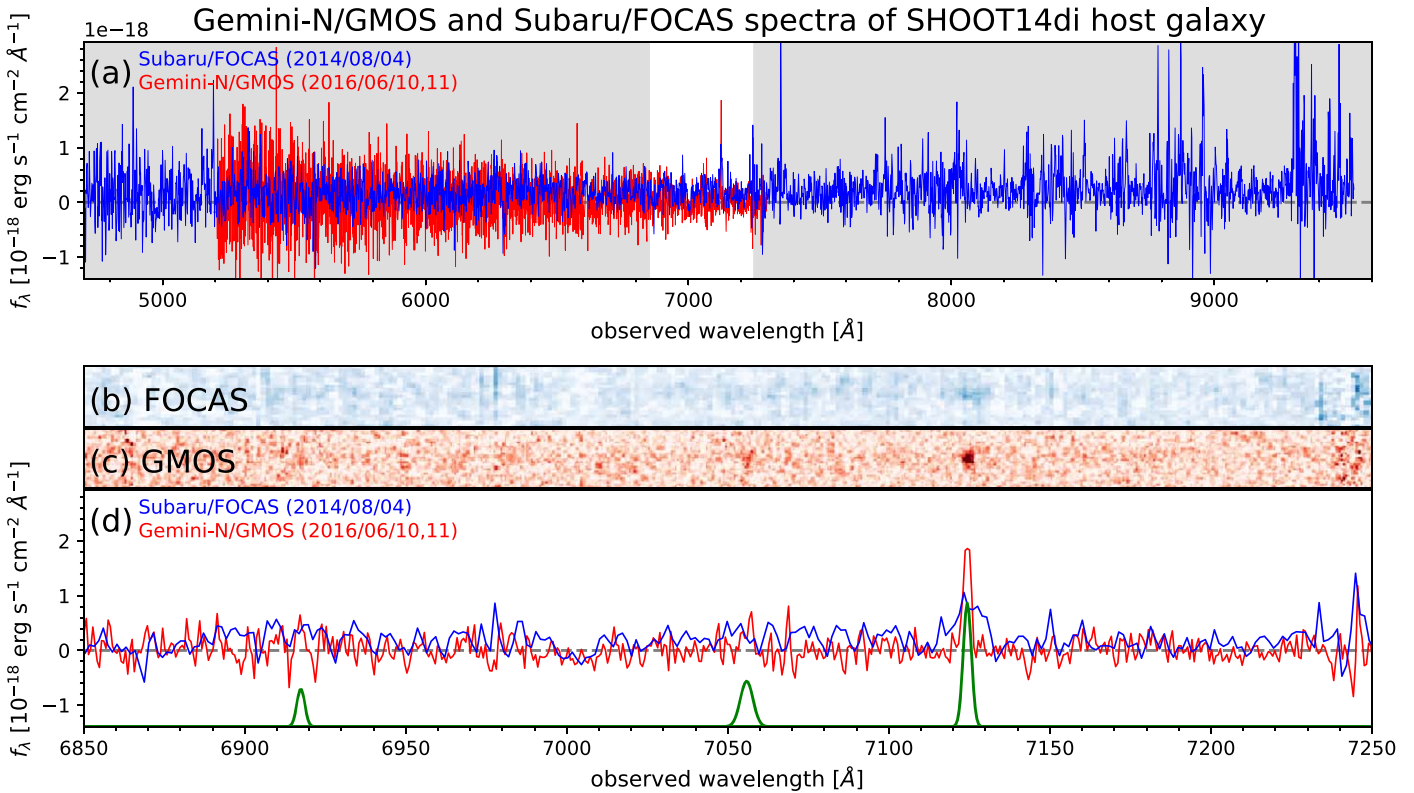


Figure 4. Observed spectra of the host galaxy of SHOOT14di with Gemini-North GMOS (red) and Subaru FOCAS (blue). Best-fitted Gaussian for the $H\beta$ and two $[O III]$ lines are shown in green, although the detection of $H\beta$ line is marginal. (a) The spectra in almost the entire range of the FOCAS spectrum. (b) and (c) Magnified views of the two-dimensional FOCAS and GMOS spectra, respectively. (d) A magnified view of the 1D spectra around the detected emission lines.

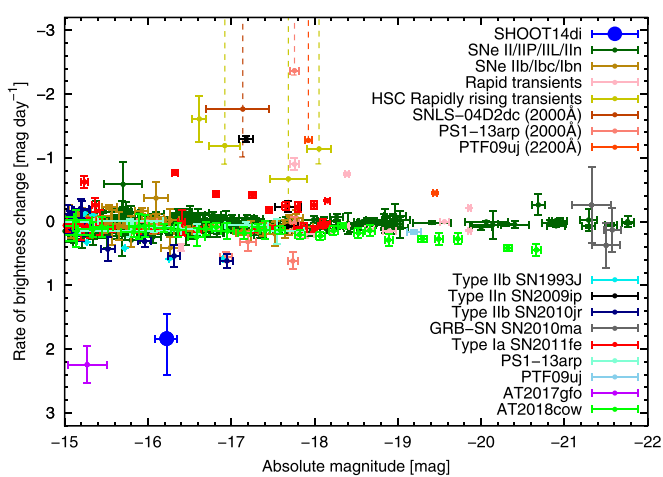


Figure 5. Absolute magnitudes and rates of brightness change of SHOOT14di (blue) compared with those of shock breakouts (SNLS-04D2dc (dark orange, Schawinski et al. 2008; Gezari et al. 2008); PS1-13arp (salmon, Gezari et al. (2015) and PTF 09uj (orange-red, Ofek et al. (2010); other SNe (Type Ia SN 2011fe (red, Nugent et al. 2011; Brown et al. 2012; Type IIb SN 1993J (cyan, Richmond et al. 1994, 1996; Type IIc SN 2009ip (black), Type IIb SN 2010jr (navy), Type II/IIIP/IIIL/IIIn SNe (dark green), Type IIb/Ibc/Ibn SNe (dark goldenrod), Pritchard et al. 2014), rapid transients (light-pink, Drout et al. 2014), rapidly rising transients (dark yellow, Tanaka et al. 2016), AT2017gfo (dark magenta, Villar et al. 2017 and references therein), and AT2018cow (green, Prentice et al. 2018; Perley et al. 2019). The absolute magnitudes and rates of brightness change of PS1-13arp (aquamarine) and PTF 09uj (sky blue) at the phases other than the shock breakout are also shown. These values are K -corrected to $\lambda_{rest} = 3400 \text{ \AA}$, except for the shock breakout of SNLS-04D2dc, PS1-13arp, and PTF 09uj. The data of PS1-13arp on MJD = 56401.01 is excluded from the analysis because of the short exposure time (S. Gezari 2019, private communication).

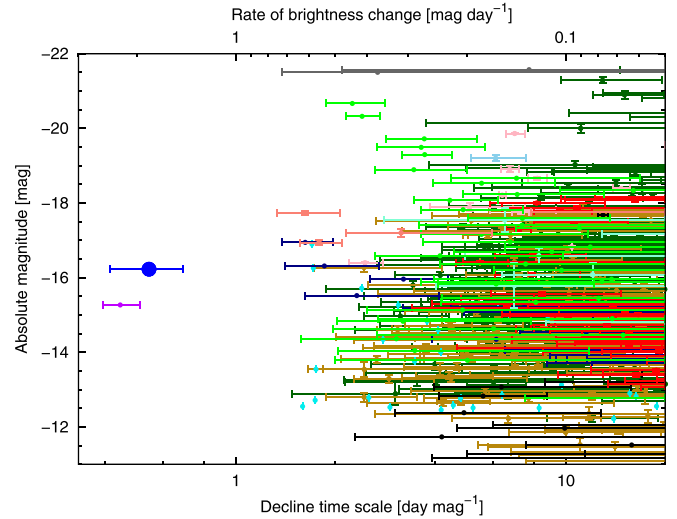


Figure 6. Decline timescales and absolute magnitudes of SHOOT14di, other SNe, rapid transients, rapidly rising transients, and a kilonova. The colors of points are the same as Figure 5.

For our transient search, the HSC data are reduced using HSC pipeline¹⁶ (Bosch et al. 2018) version 3.6.1, which is based on the LSST pipeline (Ivezic et al. 2008; Axelrod et al. 2010). It provides packages for bias subtraction, flat fielding, astrometry, flux calibration, mosaicing, warping, coadding, and image subtraction. The astrometry and photometry are made

¹⁶ A prototype is described in Furusawa et al. (2010).

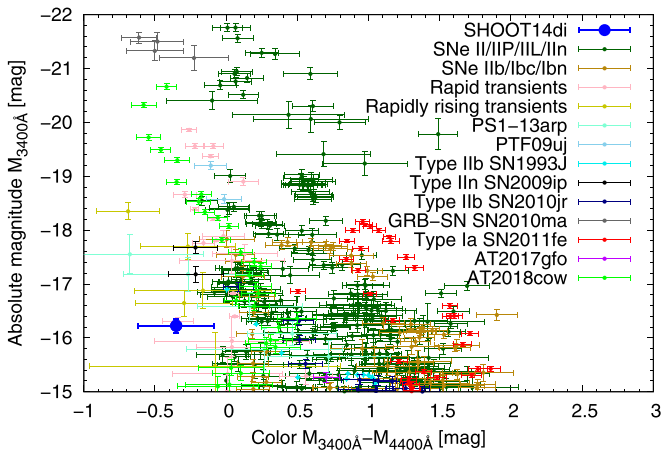


Figure 7. Color–magnitude diagram of SHOOT14di (blue), other SNe, rapid transients, rapidly rising transients, and a kilonova, except for the shock breakout of SNLS-04D2dc, PS1-13arp, and PTF 09uj. The colors of points are the same as in Figure 5.

relative to the Sloan Digital Sky Survey (SDSS) DR8 (Aihara et al. 2011) with a $2''.36$ (14 pixel) diameter aperture. We developed a quick image-subtraction system with the HSC pipeline and performed real-time transient finding (Tominaga et al. 2014a), in cooperation with an on-site data analysis system (Furusawa et al. 2011, 2018). This enables us to report numerous SN candidates immediately after the observing runs (Tominaga et al. 2014a, 2014b, 2015a, 2015b), and to search for optical counterparts of gravitational waves and fast radio bursts (Tominaga et al. 2018a, 2018b; Utsumi et al. 2018). On the other hand, the image subtractions between the HSC images and the FOCAS images are made with HOTPANTS version 5.1.10 (Becker 2015) after warping the HSC images with WCSREMAP. For these image subtractions, the difference imaging method of Alard & Lupton (Alard & Lupton 1998; Alard 2000) is adopted, which handles point-spread function (PSF) variations and allows successful image subtraction between images with different PSF sizes.

To detect candidates with short time variabilities, the first g - and r -band images obtained on Day 1 are set as reference images for the image subtraction. Objects with more than one detection at significance higher than 5σ in the difference images are selected as rapid transient candidates. In other words, the candidates show variability between observations on two successive nights. On the other hand, for the photometry, we adopt images taken on Day 327 and Day 414 as reference images for the g and r bands, respectively, and subtract the reference images from hourly stacked and daily-stacked images of Days 1 and 2. We evaluate astrometric accuracy in the difference images by a random injection of artificial point sources to images before warping, coadding, and image subtraction. After warping, coadding, image subtraction, and source detection, the positions of artificial sources with 25–25.5 mag are recovered to a median accuracy of $<0''.14$. The fluxes are measured with aperture photometry using a $2''.36$ diameter aperture on the difference images (Figures 2(a) and 2(b)).

2.2. Imaging Observations of the Host Galaxy

In addition to the g -band observation with HSC on Day 327 and the r -band observation with HSC on Day 414, we performed r' -, i' -, and Y -band imaging observations with

Suprime-Cam (Miyazaki et al. 2002) on 2016 May 7 (UT) (Day 676) to derive properties of a host galaxy at R.A. = $21^{\text{h}}33^{\text{m}}04^{\text{s}}.30$, decl. = $+09^{\circ}35'54''.9$ (J2000.0) (Figure 3). For the multiband photometry of the host galaxy, we adopt HSC pipeline version 4.0.1 to derive consistently composite model (CModel) fluxes with exponential and de Vaucouleurs fits.¹⁷ The imaging observations and photometry of a host galaxy are summarized in Table 2. As the pixel scales of Suprime-Cam and HSC are different, the multiband data analysis is performed separately for the Suprime-Cam and HSC images. The discrepancy between the r -band flux with an HSC image and the r' -band flux with a Suprime-Cam image is taken into account as a systematic error in the subsequent analysis. The position of host galaxy is also derived from the multiband analyses (Bosch et al. 2018). The position in each image is measured by an approximate maximum-likelihood algorithm implemented in the HSC pipeline (Bosch et al. 2018, see also Pier et al. 2003). The method gives a median root-mean-square of $<0''.1$ at a seeing of $<2''$ in the SDSS with a pixel scale of $0''.396$ (Pier et al. 2003). We adopt the average position of the host galaxy derived by the multiband analyses of the HSC images and the Suprime-Cam images. These multiband analyses give a consistent position of the host galaxy within $0''.14$.

2.3. Spectroscopic Observation

Optical spectroscopic observations were carried out with FOCAS on the 8.2 m Subaru telescope on 2014 August 5 (Day 35) and with the Gemini Multi-Object Spectrograph (GMOS; Hook et al. 2004) on the 8.1 m Gemini-North telescope on 2016 June 10 and 11 (Days 710 and 711).

In the FOCAS observation, we aimed to take a spectrum of the transient and took four 20 minute exposures. Low-resolution spectra ($R \sim 600$) were obtained in the multi-object slit mode with the $0''.8$ -width slit, 300 lines mm^{-1} blue (300B) grism, and the SY47 order-sort filter, providing wavelength coverage of 4700–9000 Å. We adopted the 2×1 binning mode in spatial and spectral directions, respectively. The obtained spatial and spectral samplings are $0''.208 \text{ pixel}^{-1}$ and 1.4 Å pixel^{-1} , respectively. A standard star, BD+28d4211, was observed on the same night in the same observing mode and is used for flux calibration. The data are reduced with the IRAF packages (Tody 1986, 1993) in a standard manner.

In addition, we took four 22.5 minute exposures with GMOS to take the host galaxy spectrum on 2016 June 10 and 11. A medium-resolution spectrum ($R \sim 3000$) was obtained in the long-slit mode with the $0''.75$ -width slit, 831 lines mm^{-1} (R831_G5302) grism, and the GG455_G0305 order-sort filter, providing the wavelength coverage of 5200–7300 Å. We adopted the 2×2 binning mode and the obtained spatial and spectral samplings are $0''.145 \text{ pixel}^{-1}$ and $0.67 \text{ Å pixel}^{-1}$, respectively. We stacked the four spectra after removing cosmic rays from each two-dimensional spectrum. We use a standard star, Feige 34, for flux calibration, based on observations taken on 2016 April 24 in a different configuration, with the same grism and no order-sort filter. The effects on our flux calibration of these different configurations for the target and the standard star are evaluated in the next paragraph. The data are reduced with the GEMINI-IRAF reduction software package in a standard manner.

¹⁷ <http://www.sdss.org/dr12/algorithms/magnitudes/#cmodel>

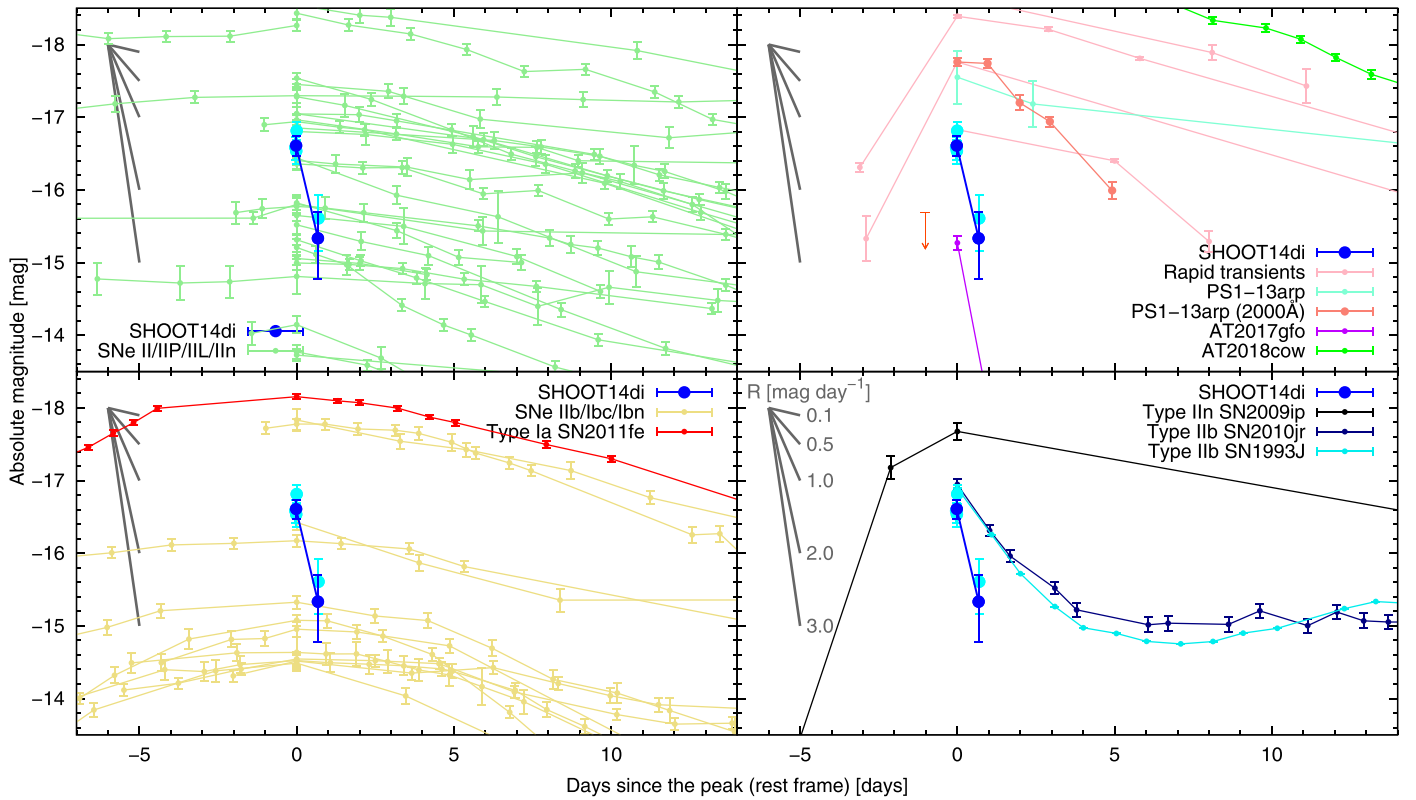


Figure 8. Light curve of SHOOT14di (blue) compared with those of SNe II/IIP/IIL/IIn (top left), rapid transients, PS1-13arp, AT2017gfo, and AT2018cow (top right), SNe Ia/Ib/Ibc/Ibn (bottom left), and Type IIn SN 2009ip, Type Ib SN 2010jr, and Type Ib SN 1993J (bottom right).

The slit of the GMOS spectrum as well as that of the FOCAS spectrum was aligned with a nearby bright star, SDSS J213304.29+093551.6. The SDSS r -band magnitude is $r = 20.60 \pm 0.03$ according to SDSS DR14. The GMOS spectrum of this star is well matched with an M1-type star. An apparent r -band magnitude of the star obtained by convolving the observed spectrum with the SDSS r -band response function is 21.16 mag and the difference of the magnitudes is 0.56 mag, corresponding to a factor of 1.67 in brightness. This is attributed to the different order-sorting filters between the target and standard star, slit losses, and atmospheric extinction. As observed line fluxes of the host galaxy measured in Section 3.2 are likely to be lost as the flux of SDSS J213304.29+093551.6 does, they are multiplied by a factor of 1.67.

3. Observational Properties

3.1. SHOOT14di

Figure 1 shows the multicolor images constructed from the g - and r -band images taken with HSC, the monochromatic g - and r -band images taken with HSC and FOCAS, and the difference images after the image subtraction. An object with decline between Days 1 and 2 is found in the g band at $0''.44$ west and $0''.14$ north of the host galaxy. The full width at half maximum size of the host galaxy is $1''.10$ in the r band image taken on Day 2.

The g -band fluxes on Days 1 and 2 are ~ 0.28 – 0.36 and $\sim 0.1 \mu\text{Jy}$, respectively. The flux measurement with the g -band daily-stacked images also gives consistent results. The g -band flux declines at a rate of $-0.204 \pm 0.052 \mu\text{Jy day}^{-1}$, corresponding to $+1.28^{+0.40}_{-0.27} \text{ mag day}^{-1}$ in the observer frame between Days 1 and 2. Here, the error is evaluated with a geometric mean

of the 1σ flux errors. The r -band flux on Day 1 is $0.21 \mu\text{Jy}$. On the other hand, nothing is significantly detected in the difference image between the r -band images taken on Days 2 and 414, or in the difference image between the FOCAS and HSC images. The 3σ upper limits on Day 35 are $0.27 \mu\text{Jy}$ in the g band and $0.30 \mu\text{Jy}$ in the r band (using a $2''.36$ diameter aperture). The fluxes are summarized in Table 1, and the g - and r -band light curves are shown in Figures 2(a) and (b). Here, the Galactic reddening is corrected with a color excess $E_{B-V, \text{Gal}}$ of 0.036 mag (Schlafly & Finkbeiner 2011)¹⁸ and a fitting function of the Galactic extinction curve (Pei 1992).

To characterize time variability, we introduce a rate of brightness change $R(\lambda_{\text{rest}}, \Delta t_{\text{rest}})$ at a wavelength λ_{rest} within an interval Δt_{rest} in the rest frame. For SHOOT14di at $z = 0.42285$ (Section 3.2), 1 day in the observer frame corresponds to $\Delta t_{\text{rest}} = 0.70$ day, and the effective rest wavelength is 3400 \AA for the g band. The observations illustrate that $R(3400 \text{ \AA}, 0.70 \text{ day})$ of SHOOT14di between Days 1 and 2 is $-0.294 \pm 0.074 \mu\text{Jy day}^{-1}$. The rate at $\lambda_{\text{rest}} = 3400 \text{ \AA}$ is also written in terms of magnitude as $R(3400 \text{ \AA}, 0.70 \text{ day}) = +1.83^{+0.57}_{-0.39} \text{ mag day}^{-1}$.

3.2. Host Galaxy

The FOCAS spectrum taken on Day 35 does not show any SN features, which is reasonable considering the depth of the spectroscopic observations and the faintness of the transient on that day. We detected an emission line on the faint continuum from the host galaxy at 7124.4 \AA . The second spectrum taken with GMOS focused on the wavelength region around this single

¹⁸ <http://irsa.ipac.caltech.edu/applications/DUST/>

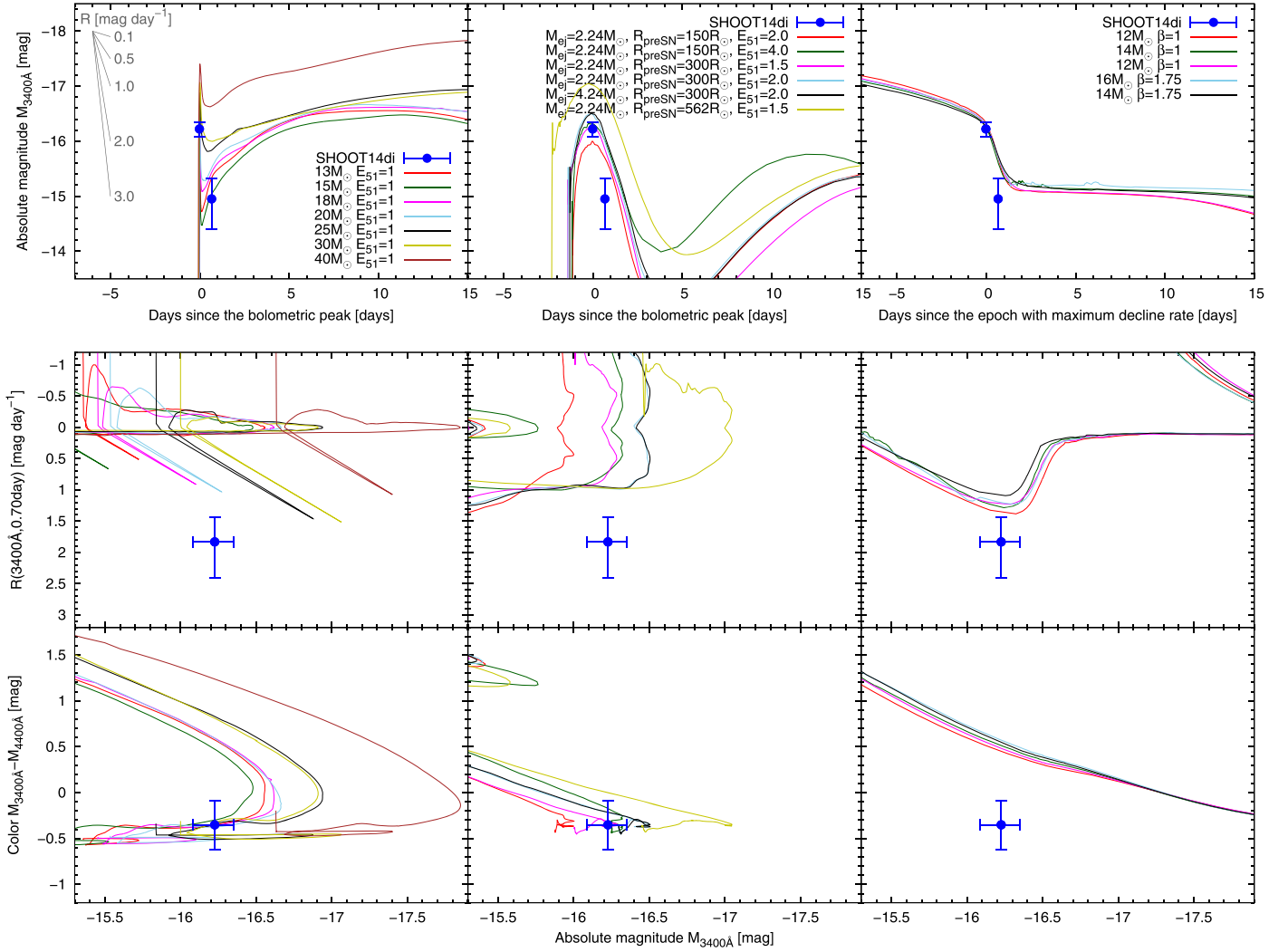


Figure 9. Light curve (top), rate of brightness change (middle), and color (bottom) of SHOOT14di (blue) compared with those of theoretical models of a shock breakout at the stellar surface of SN IIP (left), a cooling envelope emission of SN IIb (middle), and an explosion of red supergiant star with a dense circumstellar wind with $E_{s1} = 0.5$, the mass-loss rate of $10^{-2} M_{\odot} \text{ yr}^{-1}$, and the outer radius of dense wind of 10^{15} cm (right).

emission line. Thanks to the higher resolution of the GMOS spectrum, we successfully detected another emission line at 7056.2 \AA , as shown in Figure 4. These two emission lines correspond to the [O III] doublet $\lambda\lambda 5007, 4959$ at $z = 0.4229$. The *gr* HSC and *r'i'Y* Suprime-Cam broad-band photometry is fitted by a Bayesian photometric-redshift code (Tanaka 2015) with the redshift fixed to the spectroscopic redshift to infer the stellar mass of the galaxy. Using the Bruzual & Charlot (2003) stellar population synthesis models for the Chabrier initial mass function (Chabrier 2003), we find that the galaxy is a low-mass galaxy with $M_{*} = 1.2 \times 10^8 M_{\odot}$. The code applies priors on the physical properties of galaxies such as star formation rate, stellar mass, age, and dust extinction, but the inferred stellar mass does not significantly change if we disable all the priors. The typical statistical uncertainty in the stellar mass is 0.2–0.3 dex when the redshift is fixed (Tanaka 2015). This level of uncertainty does not affect the following discussions.

The combined line flux of the two [O III] emission lines is $6.0 \times 10^{-18} \text{ erg s}^{-1} \text{ cm}^{-2}$. Our detection of the $H\beta$ emission line is marginal. The Gaussian-fitted and 3σ upper limits of $H\beta$ line flux are $1.4 \times 10^{-18} \text{ erg s}^{-1} \text{ cm}^{-2}$ and $2.8 \times 10^{-18} \text{ erg s}^{-1} \text{ cm}^{-2}$, respectively. The [O II] emission line at

this redshift is not detected and only a weak upper limit of $1.0 \times 10^{-17} \text{ erg s}^{-1} \text{ cm}^{-2}$ (3σ) can be set. The lower limit of the flux ratio of $\log_{10}\{f([\text{O III}])/f(H\beta)\} = +0.82$ roughly corresponds to a metallicity of $12 + \log_{10}(\text{O}/\text{H}) \sim 7.7 - 8.3$ (Nagao et al. 2006). Although [O III] emission lines are not a good proxy for measuring the star formation rate of a galaxy in general, we use them here to put a constraint on the star formation rate of the host galaxy. We adopt a typical $\log_{10}([\text{O III}]/H\beta)$ line flux ratio of $\sim +0.6$ (Juneau et al. 2014) to convert the [O III] flux to $H\beta$ flux, which is roughly consistent with our measurements. Given the small stellar mass derived from the photometric-redshift code, we expect the dust extinction to be small or almost zero (Garn & Best 2010). Then, assuming case B recombination and zero extinction, we obtain an $H\alpha$ line luminosity of $3.8 \times 10^{39} \text{ erg s}^{-1}$ and star formation rate of $0.03 M_{\odot} \text{ yr}^{-1}$ (Kennicutt et al. 1994). Taking into account the extended nature of the host galaxy inferred from the difference between its Kron and PSF magnitude, its absolute flux density could be about three times larger than the current estimate, resulting in the star formation rate of $\sim 0.1 M_{\odot} \text{ yr}^{-1}$. A ratio of the faint $H\alpha$ emission line luminosity and faint absolute broad-band

magnitude roughly follows previous results on H α emitting galaxies (Tresse et al. 2002).

4. Comparisons with Known Transients and Variables

4.1. Supernovae, Rapid Transients, and a Kilonova

The peak magnitude, time variability, and color of SHOOT14di are compared with SNe, rapid transients recently pointed out by Drout et al. (2014), and a kilonova found in 2017 (Abbott et al. 2017). Figure 5 shows the rate of brightness change at $\lambda_{\text{rest}} \sim 3400 \text{ \AA}$ as a function of the absolute magnitude (based on the brighter of the two observations used for the rate estimate), while Figure 6 shows the absolute magnitude at $\lambda_{\text{rest}} \sim 3400 \text{ \AA}$ as a function of the timescale of the variability. Figure 7 is a color–magnitude diagram with an absolute magnitude $M_{3400 \text{ \AA}}$ at $\lambda_{\text{rest}} \sim 3400 \text{ \AA}$ and a color, $M_{3400 \text{ \AA}} - M_{4400 \text{ \AA}}$, derived with magnitudes at $\lambda_{\text{rest}} \sim 3400$ and $\sim 4400 \text{ \AA}$. Figure 8 shows comparisons of light curves at $\lambda_{\text{rest}} \sim 3400 \text{ \AA}$ with the other transients. The rate and color–magnitude diagram of other SNe and transients is derived from the u - and b -band light curves of nearby SNe obtained by the *Swift* Ultraviolet/Optical Telescope (Nugent et al. 2011; Brown et al. 2012; Pritchard et al. 2014), the U - and B -band light curves of SN 1993J (Richmond et al. 1994, 1996), the g - and r -band light curves of PTF 09uj after the shock breakout obtained by PTF (Ofek et al. 2010), the g - and r -band light curves of PS1-13arp after the shock breakout and rapid transients obtained by *Pan-STARRS1* (Gezari et al. 2015; Drout et al. 2014), the g - and r -band light curves of the rapidly rising transients obtained by *HSC* (Tanaka et al. 2016), $uvw1$ -, u -, and g -band light curves of a fast luminous ultraviolet transient AT2018cow (Prentice et al. 2018; Perley et al. 2019), and U -, g -, and r -band light curves of a kilonova (AT2017gfo) associated with a gravitational wave source GW170817 (Andreoni et al. 2017; Arcavi et al. 2017; Coulter et al. 2017; Cowperthwaite et al. 2017; Díaz et al. 2017; Drout et al. 2017; Evans et al. 2017; Kasliwal et al. 2017; Pian et al. 2017; Shappee et al. 2017; Smartt et al. 2017; Utsumi et al. 2017; Valenti et al. 2017, summarized in Villar et al. 2017). We apply K -corrections by interpolating or extrapolating their spectral energy distributions in magnitude. We also calculate the lower limits of the rise rates of SNLS-04D2dc, PTF 09uj, and PS1-13arp with 3σ upper limits at 1 day or 2 days before their detection and the rate of brightness change of PTF 09uj and PS1-13arp from their NUV light curves obtained with the *GALEX* satellite; however, K -corrections are not applied to the NUV light curves of SNLS-04D2dc, PTF 09uj, and PS1-13arp because there are no simultaneous observations with high signal-to-noise ratios in other bands.

Figures 5–8 illustrate following characteristics of SHOOT14di:

1. All of SNe and SLSNe decline more slowly than SHOOT14di. The colors of most of them are redder than that of SHOOT14di ($M_{3400 \text{ \AA}} - M_{4400 \text{ \AA}} \sim -0.4$). The transient most similar to SHOOT14di is the cooling tail of the shock breakout of SNe I Ib. However, its brightness change is half as fast as that of SHOOT14di.
2. The colors of the GRB-associated Type Ic SN 2010ma and the shock breakout in the dense circumstellar wind of PTF 09uj are similar to that of SHOOT14di. The absolute rate of brightness change of PTF 09uj at the first NUV detection is consistent with that of SHOOT14di.

However, their brightness is brighter than that of SHOOT14di and the rate of brightness change of PTF 09uj is slower than that of SHOOT14di at the same brightness.

3. The colors of rapid transients at their peak are as blue as that of SHOOT14di and their brightness is also consistent with SHOOT14di. However, their decline is slow in spite of their rapid rise. Drout et al. (2014) indicate that their decline timescales $t_{1/2, \text{decline}}$ are $t_{1/2, \text{decline}} \gtrsim 2$ days, corresponding to $R(0.7 \text{ day}) \lesssim +0.26 \text{ mag day}^{-1}$, which is slower than SHOOT14di.
4. The lower limit of the temperature of PS1-13arp at its earliest epoch ($T > 2.2 \times 10^4 \text{ K}$) indicates a blue color of PS1-13arp ($M_{3400 \text{ \AA}} - M_{4400 \text{ \AA}} < -0.11 \text{ mag}$), which is consistent with that of SHOOT14di. The color and brightness of PS1-13arp just after the shock breakout are also consistent with that of SHOOT14di, and the absolute rate of brightness change of PS1-13arp at the first NUV detection is consistent with that of SHOOT14di. However, the decline rate of PS1-13arp just after the peak, even in the NUV band, ($R(2000 \text{ \AA}, 0.7 \text{ day}) = +0.62 \pm 0.13 \text{ mag day}^{-1}$) is slower than that of SHOOT14di in the optical bands.
5. The absolute rate of brightness change of SNLS-04D2dc at the first NUV detection is consistent with that of SHOOT14di. Unfortunately, the decline rate of SNLS-04D2dc cannot be well constrained owing to its low signal-to-noise ratios.
6. The absolute rate of brightness change and color of rapidly rising transients reported in Tanaka et al. (2016) are similar to those of SHOOT14di. The origin of the rapid rise is suggested to be emission by a cooling envelope or the shock breakout in a dense circumstellar wind, depending on the brightness and the rise rate. Unfortunately, there are no observation of their decline.
7. While the color of AT2018cow at its peak is consistent with that of SHOOT14di, AT2018cow is redder than SHOOT14di at the same brightness. The rates of brightness change of AT2018cow are $R(3400 \text{ \AA}, 0.70 \text{ day}) \sim +0.44 \text{ mag day}^{-1}$ at the peak and $R(3400 \text{ \AA}, 0.70 \text{ day}) \sim +0.15 \text{ mag day}^{-1}$ at $M_{3400 \text{ \AA}} = -16$. Both rates are slower than that of SHOOT14di.
8. The brightness change of SHOOT14di is as rapid as that of AT2017gfo. However, the peak magnitude and color of SHOOT14di is 1 mag brighter and 1 mag bluer than those of AT2017gfo, respectively.

The discovery of the rapidly declining Type I SN 2019bkc/ATLAS19dqr has recently been reported (Chen et al. 2019). In the observer frame, SN 2019bkc exhibits slower decline rates, $+0.45$ to $+0.63 \text{ mag day}^{-1}$ in the B -, V -, g -, r -, and i -bands, and a redder color at the peak, than SHOOT14di. Although the absolute brightness, the rates, and the color in the rest frame of SN 2019bkc cannot be constrained because it appears to be hostless, the origin of SN 2019bkc is likely to be different from that of SHOOT14di.

4.2. Other Transients or Variables

There are other transients or variables with timescales shorter than SNe and similar transients. In this section, we review their properties and compare them to those of SHOOT14di.

Considering the astrometric accuracy for the positions of artificial sources in the difference images and the position of host galaxy (Sections 2.1 and 2.2), SHOOT14di appeared at the outskirts of the host galaxy and thus is unlikely to be an active galactic nucleus or a tidal disruption event. We rule out an asteroid because the displacement between Days 1 and 2 is less than $0''.17$ and no variable, i.e., moving, object is found within 1 arcmin around SHOOT14di on Day 327.

The decline rate of SHOOT14di could be reproduced with the optical flash and afterglow of an on-axis GRB, or the orphan afterglow of an off-axis GRB. However, SHOOT14di is continuously bright over ≥ 56 minutes in the rest frame on Day 1, which is longer than the typical duration of on-axis GRBs, and there were no alerts of GRBs at the location of SHOOT14di on Days 1 and 2. On the other hand, the duration on Day 1 and the decline rate between Days 1 and 2 could be explained by a GRB orphan afterglow peaking at ~ 0.6 – 1.4 days, depending on the power-law index α of light-curve decline, where $F \propto t^{-\alpha}$. Here we adopt $\alpha = 1.6$ – 3.0 (e.g., Granot et al. 2002; Totani & Panaitescu 2002). The early peak of the GRB orphan afterglow and the nondetection of on-axis GRBs require a viewing angle θ_{obs} of $\theta_{\text{jet}} < \theta_{\text{obs}} \lesssim 7^\circ$ for the opening angle θ_{jet} of $\theta_{\text{jet}} \lesssim 4^\circ$, or $\theta_{\text{jet}} < \theta_{\text{obs}} \lesssim \theta_{\text{jet}} + 2^\circ$ for $6^\circ \lesssim \theta_{\text{jet}} \lesssim 14^\circ$. The solid angle required for GRB orphan afterglows by the early peak is similar to that for the on-axis GRBs, and thus their occurrence rates are likely to be comparable. Adopting the cosmic GRB rate (Lien et al. 2014), the expected occurrence number of GRB orphan afterglows with an early peak during the HSC observation on Days 1 and 2 is $\lesssim 0.001$ for GRBs at $z \leq 2$. The number is much smaller than unity, thus a serendipitous detection is unlikely. Furthermore, the optical spectrum of the GRB afterglow is proportional to $\nu^{-1/2}$ at ~ 1 day (Sari et al. 1998; Granot et al. 2002), thus the color of the GRB orphan afterglow ($M_{3400 \text{ \AA}} - M_{4400 \text{ \AA}} \sim +0.14$) is redder than that of SHOOT14di.

Another possible candidate is a chance projection of the flare of a low-mass Galactic star. As SHOOT14di was detected on Days 1 and 2, and the typical duration of flare is ~ 20 minutes, two flares with durations of ≥ 1.34 hr and ≥ 2.16 hr are required to explain the decline rate of SHOOT14di. The occurrence rate of flares is $\sim 2 \text{ hr}^{-1} \text{ deg}^{-2}$ in the observed field with the Galactic coordinate $(l, b) = (62^\circ 30', -29^\circ 53')$ (Kowalski et al. 2009). The *Kepler* satellite has provided statistical features of the flares of dwarf stars; the number of flares with $t \geq 20$ minutes is proportional to t^{-2} (Davenport et al. 2014). The expected occurrence number of two flares somewhere in the field during the HSC observing run is ~ 0.018 . The possibility is further reduced with a condition that these flares take place at the position of the distant galaxy. Therefore, a set of flares unlikely reproduce SHOOT14di.

5. Comparisons with Theoretical Models

As there are no known transients or variables that are consistent with the peak luminosity, decline rate, and color of SHOOT14di, we compare these properties of SHOOT14di with published theoretical models suggested for objects with a rapid rise and/or decline: (1) shock breakout at the stellar surface of SN IIP (Tominaga et al. 2011); (2) emission by the cooling envelopes of SN IIB (Tsvetkov et al. 2012); and (3) the explosion of red supergiant star with a dense circumstellar wind (Moriya et al. 2018). All models are calculated with the

multigroup radiation hydrodynamics code STELLA (Blinnikov et al. 2006), and the synthetic spectral energy distribution is convolved with the CCD quantum efficiency, transmittance of the dewar window and the Primary Focus Unit, and filter transmission curves of HSC.¹⁹

Figure 9 shows comparisons between SHOOT14di and the theoretical models at epochs with absolute magnitudes similar to that of SHOOT14di ($M_{3400 \text{ \AA}} \sim -16.2$ mag) and with similar $R(3400 \text{ \AA}, 0.70 \text{ day})$. The high decline rate with $M_{3400 \text{ \AA}} \sim -16.2$ mag is realized in the decline after the shock breakout peak and the cooling envelope peak immediately after the explosion for mechanisms (1) and (2), respectively, while it is achieved in the decline immediately after the forward shock breaks out from a dense wind with a high mass-loss rate of $10^{-2} M_\odot \text{ yr}^{-1}$ for mechanism (3) (top panels of Figure 9).

Middle panels of Figure 9 show $R(3400 \text{ \AA}, 0.70 \text{ day})$ as a function of $M_{3400 \text{ \AA}}$. The rates of brightness change with $M_{3400 \text{ \AA}} \sim -16.2$ mag are as high as $\sim +1 \text{ mag day}^{-1}$ for mechanisms (1) and (2) and $\sim +1.4 \text{ mag day}^{-1}$ for mechanism (3). These are all slightly slower than that of SHOOT14di. The bottom panels of Figure 9 show $M_{3400 \text{ \AA}} - M_{4400 \text{ \AA}}$ as a function of $M_{3400 \text{ \AA}}$. The color and absolute magnitude of SHOOT14di is reproduced with mechanisms (1) and (2), while the color of mechanism (3) is 0.8 mag redder than SHOOT14di. The large color difference indicates that mechanism (3) is not the origin of SHOOT14di.

The middle panel of Figure 9 demonstrates that the decline rate of mechanism (2) is independent on the explosion energy and the presupernova radius. The rate of brightness change of $R(3400 \text{ \AA}, 0.70 \text{ day}) \sim +1 \text{ mag day}^{-1}$ is consistent with those of SNe IIB observed to date (Section 4.1), and slower than that of SHOOT14di, although the decline rate could be higher if relativistic corrections are taken into account (Tolstov et al. 2013). The influence of relativistic corrections requires more detailed radiative transfer modeling from optically thin (transparent) to optically thick (diffusion) regions and should be studied elsewhere.

On the other hand, a rate of brightness change as high as $R(3400 \text{ \AA}, 0.70 \text{ day}) \sim +1.5 \text{ mag day}^{-1}$ appears in explosions of stars with $M_{\text{ZAMS}} = 25$ and $30 M_\odot$, corresponding to stellar radii of 1200 and $1360 R_\odot$, in mechanism (1). The top-left panel of Figure 9 demonstrates that the slow decline rate stems from the rapid rising after the decline. As the peak magnitude and the rising after the decline depend on the explosion energy, we additionally calculate properties for $25 M_\odot$ models with lower explosion energies. Figures 10 and 11 demonstrate that the peak magnitude, the decline rate, and the color of SHOOT14di are reproduced by mechanism (1) with lower explosion energies of $E \leq 0.4 \times 10^{51} \text{ erg}$. The low-energy explosions are also consistent with the nondetection of SHOOT14di on Day 35. The absolute plateau brightness of the low-energy explosions is located at the fainter side of the luminosity function of nearby SNe IIP (Richardson et al. 2014). Thus, SHOOT14di is most likely to be a shock breakout at the stellar surface of a low-energy SN IIP explosion.

6. Discussion and Conclusions

We perform a high-cadence survey with Subaru/HSC and carry out follow-up observations as part of SHOOT. In this

¹⁹ <http://www.naoj.org/Observing/Instruments/HSC/sensitivity.html>

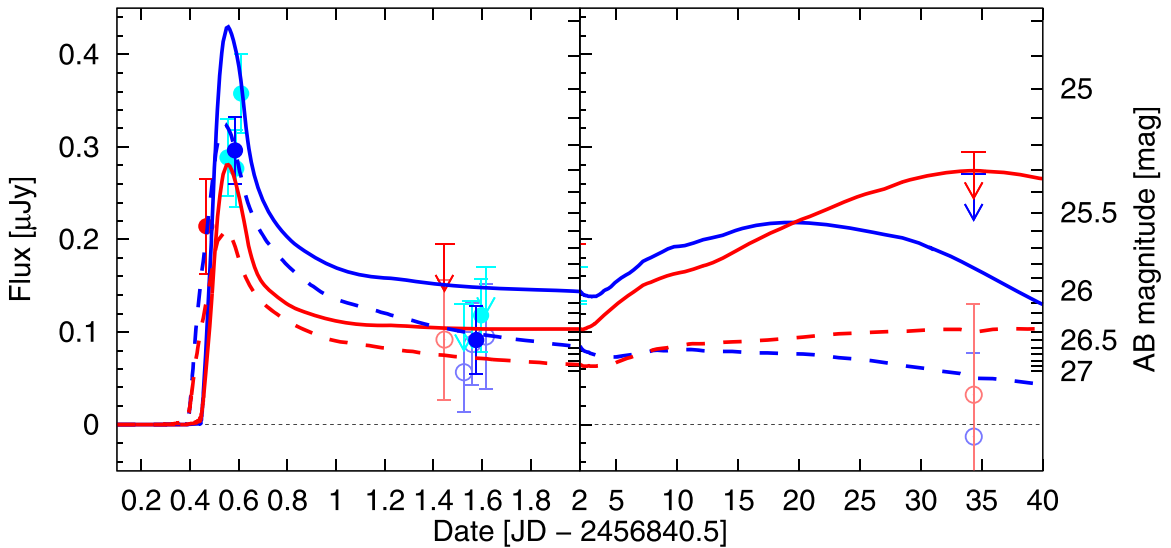


Figure 10. Comparisons between the g -band (blue) and r -band (red) light curves of SHOOT14di (symbols, same as Figure 2) and the shock breakout at the stellar surface of the low-energy explosions with $E = 0.15 \times 10^{51}$ erg (dashed lines) and $E = 0.4 \times 10^{51}$ ergs (solid lines).

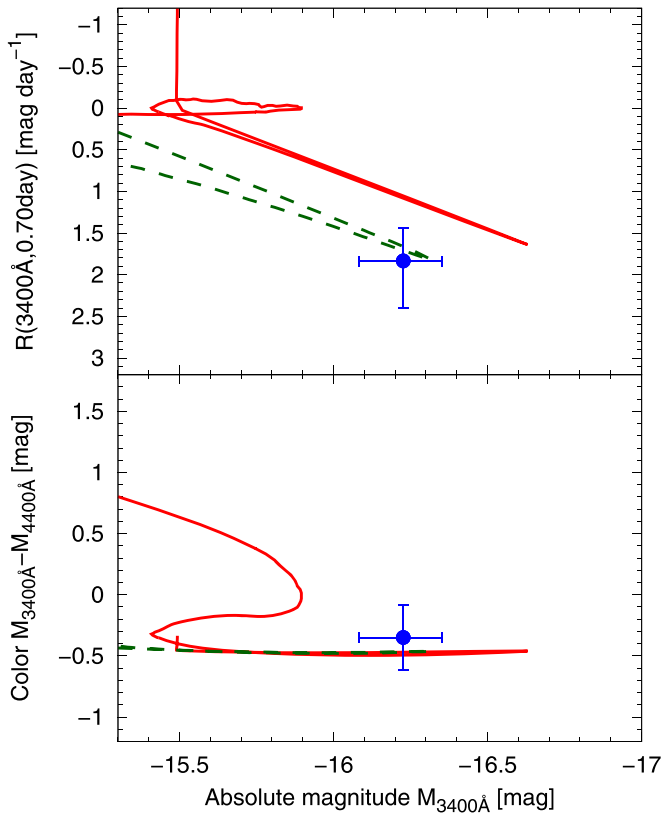


Figure 11. Rate of brightness change (top) and color (bottom) of SHOOT14di (blue) compared with those of the shock breakout at the stellar surface of the low-energy explosions with $E = 0.15 \times 10^{51}$ erg (green) and $E = 0.4 \times 10^{51}$ ergs (red).

paper, we focus on SHOOT14di which rapidly declines in observations over two successive nights.

Spectroscopic follow-up observations of the host galaxy reveal that SHOOT14di takes place at $z = 0.42285$. Based on the photometric observations, we examine the nature of SHOOT14di. SHOOT14di is unlikely to be an active galactic nucleus or a tidal disruption event because it appeared at the

outskirts of the host galaxy. The distance of SHOOT14di from the center of the host galaxy (2.5 kpc) is comparable with those of SNLS-04D2dc (~ 1.7 kpc) and PS1-13arp (4.5 kpc). The peak luminosity, decline rate, and color of SHOOT14di are inconsistent with those of SNe at >1 day after the explosions, rapid transients, AT2017gfo, AT2018cow, GRB prompt emission, or a GRB orphan afterglow. Some properties of SHOOT14di are consistent with those of some transients. For example, the decline of AT2017gfo is as fast as that of SHOOT14di and the luminosity and decline rate of SHOOT14di can be reproduced by a GRB orphan afterglow. However, AT2017gfo is fainter and redder than SHOOT14di, and a GRB orphan afterglow is redder than SHOOT14di. Furthermore, their probability of appearing in our survey expected is much smaller than unity (Section 4.2 and Scolnic et al. 2018). A set of flares of a low-mass star, which could reproduce the light curve of SHOOT14di, are unlikely to coincide with a distant galaxy.

As the observational properties of SHOOT14di are inconsistent with the known transients or variables, we compared the properties against published theoretical models calculated with STELLA: (1) shock breakout at the stellar surface of SN IIP; (2) emission by the cooling envelope of SN IIB; and (3) explosion of a red supergiant star with a dense circumstellar wind. None of them is fully consistent with SHOOT14di. They have slightly slower rates of brightness change than SHOOT14di at $M_{3400 \text{ \AA}} \sim -16.2$ mag. Furthermore, while the color of SHOOT14di is consistent with mechanisms (1) and (2), mechanism (3) gives a color redder by $+0.8$ mag than SHOOT14di.

The inconsistency between SHOOT14di and mechanism (1) can be solved with low-energy explosions of a star with $25M_{\odot}$. The multicolor light curves and color of SHOOT14di are reproduced by mechanism (1) with the SN IIP explosion of a progenitor star with $R_{\text{preSN}} = 1200R_{\odot}$ and $E \leq 0.4 \times 10^{51}$ ergs. The low-energy explosion model is consistent with the nondetection of SHOOT14di on Day 35. Thus, we suggest that SHOOT14di is the shock breakout at the stellar surface of a low-energy SN IIP explosion.

An event rate of SHOOT14di is roughly estimated by using a $1/V_{\text{max}}$ method (Schmidt 1968; Eales 1993) as done in Tanaka

et al. (2016). The event rate R is written as $R = 1/p\tau\Omega V_{\max}$, where p is a detection efficiency, τ is the longer of a rest-frame timescale of a transient τ_{tran} and a survey duration of each field $\tau_{\text{obs,field}}$, Ω is a field of view of HSC, and V_{\max} is a maximum volume per width in which a transient can be detected. Here, we assume $p = 1$ because it is difficult to evaluate p for our complicated selection criteria. The observed duration of each field in the g -band and in each night varies from 1 hr to 5.7 hr, and thus τV_{\max} can be derived from

$$\tau V_{\max} = \frac{1}{4\pi} \sum_{\text{field}} \int_0^{z_{\max}} \max \left\{ \tau_{\text{tran}}, \frac{\tau_{\text{obs,field}}}{1+z} \right\} \frac{dV}{dz} dz,$$

where z_{\max} is the maximum redshift in which a transient can be detected and $\frac{dV}{dz}$ is the comoving volume element per unit redshift. Based on the light curve of SHOOT14di, we adopt the following two cases of τ and absolute magnitude M : (1) $\tau_{\text{tran}} = 0.1$ days and $M = -16.2$ mag and (2) $\tau_{\text{tran}} = 0.7$ days and $M = -14.9$ mag. Adopting the 3σ limiting magnitude of 26.3 mag in the g -band, the resultant τV_{\max} are $\tau V_{\max} = 2.2 \times 10^{-3}$ days Gpc³ deg⁻² for case (1) and 1.9×10^{-3} days Gpc³ deg⁻² for case (2). Therefore, the event rates are 9.4×10^{-5} yr⁻¹ Mpc⁻³ for case (1) and 1.1×10^{-4} yr⁻¹ Mpc⁻³ for case (2). These are slightly lower than the core-collapse SN rate of $(3-7) \times 10^{-4}$ yr⁻¹ Mpc⁻³ at $z = 0-1$ (Dahlen et al. 2004, 2012; Botticella et al. 2008; Li et al. 2011).

According to Förster et al. (2018), taking into account the bias toward the high detectability of SNe IIP with dense CSM in their observation, one fifth of SNe IIP may exhibit shock breakout at the stellar surface. The rate of SHOOT14di is consistent with the suggestion that SHOOT14di is the shock breakout at the stellar surface of a SNe IIP. This indicates that the rapidly declining transient as SHOOT14di is a proxy for a massive star without dense CSM. The rapidly rising/declining transients are representative of massive stars with various CSM and their rates can constrain the fraction of massive stars with/without dense CSM. While rapidly rising transients have received a lot of attention recently, rapidly declining transients are also important for understanding the fate of massive stars. Although the detection of rapidly declining transients is more difficult than that of rapidly rising transients, it is important to consider a strategy to detect rapidly declining transients.

The absolute magnitude of host galaxy is $M \sim -17$ mag. This is located at the fainter end of the host galaxies of core-collapse supernovae in the local universe (Arcavi et al. 2010). The stellar mass and specific star formation rate of the host galaxy is located at the smaller and higher ends of host galaxies of core-collapse supernovae in the local universe, respectively, and the metallicity of the host galaxy is lower than the typical value of host galaxies of SNe IIP (e.g., Graur et al. 2017). SNe IIP in low-mass host galaxies with low metallicity are actually found in the local universe (e.g., Gutiérrez et al. 2018). While the star formation rate of the host galaxy of SHOOT14di is smaller than those of host galaxies of high- z core-collapse supernovae observed so far, its stellar mass and specific star formation rate are located at the lower ends of these distributions (Svensson et al. 2010). These properties of the host galaxy indicate that a core-collapse supernova can occur in it.

If SHOOT14di is the shock breakout at the stellar surface, the main-sequence mass of the best-fit model is larger than

constraints obtained for the masses of progenitors of nearby SNe IIP (Smartt 2009; Dessart et al. 2013; González-Gaitán et al. 2015). However, these observations are limited to the local universe because of the requirements of presupernova images and late nebular spectra. The main-sequence masses of SNe IIP have never been measured at a redshift as high as $z = 0.4$. The low-metallicity environment may allow a massive red supergiant star to survive until the SN explosion. Although it needs a careful treatment, due to a possible observational bias that the shock breakout is more easily detected for larger M_{ZAMS} because of larger R_{preSN} , high-cadence observations might provide a new clue to investigate the presupernova radius and M_{ZAMS} of SN progenitors outside the local universe.

The discovery of SHOOT14di and other rapidly rising transients in Tanaka et al. (2016) demonstrates that a high-cadence multicolor optical transient survey with intervals of about one hour is sensitive to high- z transients. Unfortunately, the nature of SHOOT14di and other rapidly rising transients is not well constrained due to the lack of immediate and continuous follow-up observations. Extensive high-cadence multicolor surveys together with immediate and continuous follow-up observations will provide the clue to investigate the high- z universe with short-timescale transients.


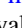

N.T. thanks Suvi Gezari for clarifying the data quality of PS1-13arp, Yuki Kikuchi, Yuki Taniguchi, and Takahiro Kato for helping the observations, and Michael W. Richmond for improving the English grammar of the manuscript. Data analyses were in part carried out on PC cluster at Center for Computational Astrophysics, National Astronomical Observatory of Japan. This research has been supported in part by the research grant program of Toyota foundation (D11-R-0830), the RFBR (19-52-50014)-JSPS bilateral program, World Premier International Research Center Initiative, MEXT, Japan, and by the Grant-in-Aid for Scientific Research of the JSPS (JP23224004, JP23540262, JP23740157, JP15H05440, JP15H02075, JP16H02166, JP17H06363) and MEXT (JP23105705). T.J.M. is supported by Japan Society for the Promotion of Science Postdoctoral Fellowships for Research Abroad (26 · 51). This work of S.Blinnikov (hydrodynamics of shock breakout and development of STELLA code) was supported by Russian Science Foundation grant 19-12-00229. This paper makes use of software developed for the Large Synoptic Survey Telescope. We thank the LSST Project for making their code available as free software at <http://dm.lsstcorp.org>. Funding for SDSS-III has been provided by the Alfred P. Sloan Foundation, the Participating Institutions, the National Science Foundation, and the U.S. Department of Energy Office of Science. The SDSS-III website is <http://www.sdss3.org/>. SDSS-III is managed by the Astrophysical Research Consortium for the Participating Institutions of the SDSS-III Collaboration including the University of Arizona, the Brazilian Participation Group, Brookhaven National Laboratory, Carnegie Mellon University, University of Florida, the French Participation Group, the German Participation Group, Harvard University, the Instituto de Astrofísica de Canarias, the Michigan State/Notre Dame/JINA Participation Group, Johns Hopkins University, Lawrence Berkeley National Laboratory, Max Planck Institute for Astrophysics, Max Planck Institute for Extraterrestrial Physics, New Mexico State University, New York University, Ohio State University, Pennsylvania State University, University of Portsmouth,

Princeton University, the Spanish Participation Group, University of Tokyo, University of Utah, Vanderbilt University, University of Virginia, University of Washington, and Yale University.

Facilities: Subaru (HSC, FOCAS), Gemini-N (GMOS-N).

Software: STELLA (Blinnikov et al. 2006), IRAF Tody (1986, 1993), Gemini-IRAF,²⁰ HSC pipeline (v3.6.1; Bosch et al. 2018), LSST pipeline (Ivezic et al. 2008; Axelrod et al. 2010), HOTPANTS (v5.1.10; Becker 2015), WCSTools (Mink 2002), Astropy (Astropy Collaboration et al. 2018), SExtractor (Bertin & Arnouts 1996).

ORCID iDs

Nozomu Tominaga  <https://orcid.org/0000-0001-8537-3153>
 Tomoki Morokuma  <https://orcid.org/0000-0001-7449-4814>
 Masaomi Tanaka  <https://orcid.org/0000-0001-8253-6850>
 Hisanori Furusawa  <https://orcid.org/0000-0002-6174-8165>
 Masayuki Tanaka  <https://orcid.org/0000-0002-5011-5178>
 Ji-an Jiang  <https://orcid.org/0000-0002-9092-5093>
 Alexey Tolstov  <https://orcid.org/0000-0002-4587-7741>
 Sergei Blinnikov  <https://orcid.org/0000-0002-5726-538X>
 Hanindyo Kuncarayakti  <https://orcid.org/0000-0002-1132-1366>
 Takashi J. Moriya  <https://orcid.org/0000-0003-1169-1954>
 Tohru Nagao  <https://orcid.org/0000-0002-7402-5441>
 Ken'ichi Nomoto  <https://orcid.org/0000-0001-9553-0685>
 Tadafumi Takata  <https://orcid.org/0000-0002-6592-4250>

References

- Abbott, B. P., Abbott, R., Abbott, T. D., et al. 2017, *ApJL*, 848, L12
 Aihara, H., Allende Prieto, C., An, D., et al. 2011, *ApJS*, 193, 29
 Alard, C. 2000, *A&AS*, 144, 363
 Alard, C., & Lupton, R. H. 1998, *ApJ*, 503, 325
 Andreoni, I., Ackley, K., Cooke, J., et al. 2017, *PASA*, 34, e069
 Arcavi, I., Gal-Yam, A., Kasliwal, M. M., et al. 2010, *ApJ*, 721, 777
 Arcavi, I., Hosseinzadeh, G., Howell, D. A., et al. 2017, *Natur*, 551, 64
 Astropy Collaboration, Price-Whelan, A. M., Sipőcz, B. M., et al. 2018, *AJ*, 156, 123
 Axelrod, T., Kantor, J., Lupton, R. H., & Pierfederici, F. 2010, *Proc. SPIE*, 7740, 15
 Becker, A. 2015, HOTPANTS: High Order Transform of PSF ANd Template Subtraction, v5.1.10, Astrophysics Source Code Library, ascl:1504.004
 Bersten, M. C., Folatelli, G., García, F., et al. 2018, *Natur*, 554, 497
 Bertin, E., & Arnouts, S. 1996, *A&AS*, 117, 393
 Blinnikov, S. I., Röpke, F. K., Sorokina, E. I., et al. 2006, *A&A*, 453, 229
 Bosch, J., Armstrong, R., Bickerton, S., et al. 2018, *PASJ*, 70, S5
 Botticella, M. T., Riello, M., Cappellaro, E., et al. 2008, *A&A*, 479, 49
 Brown, P. J., Dawson, K. S., de Pasquale, M., et al. 2012, *ApJ*, 753, 22
 Bruzual, G., & Charlot, S. 2003, *MNRAS*, 344, 1000
 Chabrier, G. 2003, *PASP*, 115, 763
 Chen, P., Dong, S., Stritzinger, M. D., et al. 2019, arXiv:1905.02205
 Chevalier, R. A., & Irwin, C. M. 2011, *ApJL*, 729, L6
 Coulter, D. A., Foley, R. J., Kilpatrick, C. D., et al. 2017, *Sci*, 358, 1556
 Cowperthwaite, P. S., Berger, E., Villar, V. A., et al. 2017, *ApJL*, 848, L17
 Dahlen, T., Strolger, L., Riess, A. G., et al. 2004, *ApJ*, 613, 189
 Dahlen, T., Strolger, L.-G., Riess, A. G., et al. 2012, *ApJ*, 757, 70
 Davenport, J. R. A., Hawley, S. L., Hebb, L., et al. 2014, *ApJ*, 797, 122
 Dessart, L., Hillier, D. J., Waldman, R., & Livne, E. 2013, *MNRAS*, 433, 1745
 Díaz, M. C., Macri, L. M., Garcia Lambas, D., et al. 2017, *ApJL*, 848, L29
 Drake, A. J., Djorgovski, S. G., Mahabal, A., et al. 2009, *ApJ*, 696, 870
 Drout, M. R., Chornock, R., Soderberg, A. M., et al. 2014, *ApJ*, 794, 23
 Drout, M. R., Piro, A. L., Shappee, B. J., et al. 2017, *Sci*, 358, 1570
 Eales, S. 1993, *ApJ*, 404, 51
 Evans, P. A., Cenko, S. B., Kennea, J. A., et al. 2017, *Sci*, 358, 1565
 Förster, F., Maureira, J. C., San Martín, J., et al. 2016, *ApJ*, 832, 155
 Förster, F., Moriya, T. J., Maureira, J. C., et al. 2018, *NatAs*, 2, 808
 Furusawa, H., Koike, M., Takata, T., et al. 2018, *PASJ*, 70, S3
 Furusawa, H., Okura, Y., Mineo, S., et al. 2011, *PASJ*, 63, 585
 Furusawa, H., Yasuda, N., Okura, Y., et al. 2010, *Proc. SPIE*, 7740, 774021
 Gal-Yam, A., Arcavi, I., Ofek, E. O., et al. 2014, *Natur*, 509, 471
 Garn, T., & Best, P. N. 2010, *MNRAS*, 409, 421
 Garnavich, P. M., Tucker, B. E., Rest, A., et al. 2016, *ApJ*, 820, 23
 Gezari, S., Dessart, L., Basa, S., et al. 2008, *ApJL*, 683, L131
 Gezari, S., Jones, D. O., Sanders, N. E., et al. 2015, arXiv:1502.06964
 González-Gaitán, S., Tominaga, N., Molina, J., et al. 2015, *MNRAS*, 451, 2212
 Graham, M. J., Kulkarni, S. R., Bellm, E. C., et al. 2019, *PASP*, 131, 078001
 Granot, J., Panaitescu, A., Kumar, P., & Woosley, S. E. 2002, *ApJL*, 570, L61
 Graur, O., Bianco, F. B., Huang, S., et al. 2017, *ApJ*, 837, 120
 Gutiérrez, C. P., Anderson, J. P., Sullivan, M., et al. 2018, *MNRAS*, 479, 3232
 Ho, A. Y. Q., Goldstein, D. A., & Sculze, S. 2019, arXiv:1904.11009
 Hook, I. M., Jørgensen, I., Allington-Smith, J. R., et al. 2004, *PASP*, 116, 425
 Ivezic, Z., Tyson, J. A., Allsman, R., et al. 2008, arXiv:0805.2366
 Juneau, S., Bournaud, F., Charlot, S., et al. 2014, *ApJ*, 788, 88
 Kashikawa, N., Aoki, K., Asai, R., et al. 2002, *PASJ*, 54, 819
 Kasliwal, M. M., Nakar, E., Singer, L. P., et al. 2017, *Sci*, 358, 1559
 Kennicutt, R. C., Jr., Tamblyn, P., & Congdon, C. E. 1994, *ApJ*, 435, 22
 Klein, R. I., & Chevalier, R. A. 1978, *ApJL*, 223, L109
 Komatsu, E., Dunkley, J., Nolte, M. R., et al. 2009, *ApJS*, 180, 330
 Kowalski, A. F., Hawley, S. L., Hilton, E. J., et al. 2009, *AJ*, 138, 633
 Law, N. M., Kulkarni, S. R., Dekany, R. G., et al. 2009, *PASP*, 121, 1395
 Li, W., Leaman, J., Chornock, R., et al. 2011, *MNRAS*, 412, 1441
 Lien, A., Sakamoto, T., Gehrels, N., et al. 2014, *ApJ*, 783, 24
 Mink, D. J. 2002, in ASP Conf. Ser. 281, *Astronomical Data Analysis Software and Systems XI*, ed. D. A. Bohlender, D. Durand, & T. H. Handley (San Francisco, CA: ASP), 169
 Miyazaki, S., Komiyama, Y., Nakaya, H., et al. 2006, *Proc. SPIE*, 6269
 Miyazaki, S., Komiyama, Y., Nakaya, H., et al. 2012, *Proc. SPIE*, 8446, 84460Z
 Miyazaki, S., Komiyama, Y., Sekiguchi, M., et al. 2002, *PASJ*, 54, 833
 Moriya, T. J., Förster, F., Yoon, S.-C., Gräffener, G., & Blinnikov, S. I. 2018, *MNRAS*, 476, 2840
 Morokuma, T., Tominaga, N., Tanaka, M., et al. 2014, *PASJ*, 66, 114
 Morozova, V., Piro, A. L., Renzo, M., & Ott, C. D. 2016, *ApJ*, 829, 109
 Morozova, V., Piro, A. L., & Valenti, S. 2017, *ApJ*, 838, 28
 Morrissey, P., Conrow, T., Barlow, T. A., et al. 2007, *ApJS*, 173, 682
 Morrissey, P., Schiminovich, D., Barlow, T. A., et al. 2005, *ApJL*, 619, L7
 Nagao, T., Maiolino, R., & Marconi, A. 2006, *A&A*, 459, 85
 Nakar, E., & Sari, R. 2010, *ApJ*, 725, 904
 Nugent, P. E., Sullivan, M., Cenko, S. B., et al. 2011, *Natur*, 480, 344
 Ofek, E. O., Rabinak, I., Neill, J. D., et al. 2010, *ApJ*, 724, 1396
 Pei, Y. C. 1992, *ApJ*, 395, 130
 Perley, D. A., Mazzali, P. A., Yan, L., et al. 2019, *MNRAS*, 484, 1031
 Pian, E., D'Avanzo, P., Benetti, S., et al. 2017, *Natur*, 551, 67
 Pier, J. R., Munn, J. A., Hindsley, R. B., et al. 2003, *AJ*, 125, 1559
 Prentice, S. J., Maguire, K., Smartt, S. J., et al. 2018, *ApJL*, 865, L3
 Pritchard, T. A., Roming, P. W. A., Brown, P. J., Bayless, A. J., & Frey, L. H. 2014, *ApJ*, 787, 157
 Rau, A., Kulkarni, S. R., Law, N. M., et al. 2009, *PASP*, 121, 1334
 Richardson, D., Jenkins, R. L., III, Wright, J., & Maddox, L. 2014, *AJ*, 147, 118
 Richmond, M. W., Treffers, R. R., Filippenko, A. V., et al. 1994, *AJ*, 107, 1022
 Richmond, M. W., van Dyk, S. D., Ho, W., et al. 1996, *AJ*, 111, 327
 Rubin, A., & Gal-Yam, A. 2017, *ApJ*, 848, 8
 Sari, R., Piran, T., & Narayan, R. 1998, *ApJL*, 497, L17
 Schawinski, K., Justham, S., Wolf, C., et al. 2008, *Sci*, 321, 223
 Schlafly, E. F., & Finkbeiner, D. P. 2011, *ApJ*, 737, 103
 Schmidt, M. 1968, *ApJ*, 151, 393
 Scolnic, D., Kessler, R., Brout, D., et al. 2018, *ApJL*, 852, L3
 Shappee, B. J., Simon, J. D., Drout, M. R., et al. 2017, *Sci*, 358, 1574
 Smartt, S. J. 2009, *ARA&A*, 47, 63
 Smartt, S. J., Chen, T.-W., Jerkstrand, A., et al. 2017, *Natur*, 551, 75
 Svensson, K. M., Levan, A. J., Tanvir, N. R., Fruchter, A. S., & Strolger, L.-G. 2010, *MNRAS*, 405, 57
 Tanaka, M. 2015, *ApJ*, 801, 20
 Tanaka, M., Tominaga, N., Morokuma, T., et al. 2016, *ApJ*, 819, 5
 Tody, D. 1986, *Proc. SPIE*, 627, 733
 Tody, D. 1993, in ASP Conf. Ser. 52, *Astronomical Data Analysis Software and Systems II*, ed. R. J. Hanisch, R. J. V. Brissenden, & J. Barnes (San Francisco, CA: ASP), 173
 Tolstov, A. G., Blinnikov, S. I., & Nadyozhin, D. K. 2013, *MNRAS*, 429, 3181

²⁰ <https://www.gemini.edu/node/11823>

- Tominaga, N., Blinnikov, S., Baklanov, P., et al. 2009, [ApJL](#), **705**, L10
- Tominaga, N., Morokuma, T., Blinnikov, S. I., et al. 2011, [ApJS](#), **193**, 20
- Tominaga, N., Morokuma, T., Tanaka, M., et al. 2014a, [ATel](#), **6291**, 1
- Tominaga, N., Morokuma, T., Tanaka, M., et al. 2014b, [ATel](#), **6763**, 1
- Tominaga, N., Morokuma, T., Tanaka, M., et al. 2015a, [ATel](#), **7565**, 1
- Tominaga, N., Morokuma, T., Tanaka, M., et al. 2015b, [ATel](#), **7565**, 1
- Tominaga, N., Niino, Y., Totani, T., et al. 2018a, [PASJ](#), **70**, 103
- Tominaga, N., Tanaka, M., Morokuma, T., et al. 2018b, [PASJ](#), **70**, 28
- Totani, T., & Panaitescu, A. 2002, [ApJ](#), **576**, 120
- Tresse, L., Maddox, S. J., Le Fèvre, O., & Cuby, J.-G. 2002, [MNRAS](#), **337**, 369
- Tsvetkov, D. Y., Volkov, I. M., Sorokina, E., et al. 2012, [PZ](#), **32**, 6
- Utsumi, Y., Tanaka, M., Tominaga, N., et al. 2017, [PASJ](#), **69**, 101
- Utsumi, Y., Tominaga, N., Tanaka, M., et al. 2018, [PASJ](#), **70**, 1
- Valenti, S., Sand, D. J., Yang, S., et al. 2017, [ApJL](#), **848**, L24
- Villar, V. A., Guillochon, J., Berger, E., et al. 2017, [ApJL](#), **851**, L21
- Waxman, E., Mészáros, P., & Campana, S. 2007, [ApJ](#), **667**, 351
- Yaron, O., Perley, D. A., Gal-Yam, A., et al. 2017, [NatPh](#), **13**, 510